

QUANTUM GASES

An Aharonov-Bohm interferometer for determining Bloch band topology

L. Duca,^{1,2} T. Li,^{1,2} M. Reitter,^{1,2} I. Bloch,^{1,2} M. Schleier-Smith,³ U. Schneider^{1,2*}

The geometric structure of a single-particle energy band in a solid is fundamental for a wide range of many-body phenomena and is uniquely characterized by the distribution of Berry curvature over the Brillouin zone. We realize an atomic interferometer to measure Berry flux in momentum space, in analogy to an Aharonov-Bohm interferometer that measures magnetic flux in real space. We demonstrate the interferometer for a graphene-type hexagonal optical lattice loaded with bosonic atoms. By detecting the singular π Berry flux localized at each Dirac point, we establish the high momentum resolution of this interferometric technique. Our work forms the basis for a general framework to fully characterize topological band structures.

More than 30 years ago, Berry (1) delineated the effects of the geometric structure of Hilbert space on the adiabatic evolution of quantum mechanical systems. These ideas have found widespread applications in physics (2) and are routinely used to calculate the geometric phase shift acquired by a particle moving along a closed path—a phase shift that is determined only by the geometry of the path and is independent of the time spent en route. Geometric phases provide an elegant description of the celebrated Aharonov-Bohm effect (3), in which a magnetic flux in a confined region of space influences the eigenstates everywhere via the magnetic vector potential. In condensed-matter physics, an analogous Berry flux in momentum space is responsible for various anomalous velocities and Hall responses (4) and lies at the heart of many-body phenomena associated with quantum Hall physics (5) and topological insulators (6). The Berry flux density (Berry curvature) is essential to the characterization of an energy band and determines its topological invariants. However, fully mapping out the geometric structure of an energy band (7–10) remains a major challenge for experiments.

Here, we demonstrate a versatile interferometric technique (9, 11) for mapping the Berry curvature of synthetic materials composed of ultracold atoms in optical lattices. In contrast to typical solid-state experiments, in which geometric effects are either averaged over the Fermi sea or largely constrained to the Fermi surface, the use of a Bose-Einstein condensate (BEC) enables measuring geometric phases along arbitrary closed paths in reciprocal space with high momentum resolution. We exploit this resolution to directly detect the topological properties of an individual Dirac cone (12) in a graphene-type hexagonal lat-

tice (Fig. 1). Concentrated at the Dirac point is a π Berry flux, which is analogous to a magnetic flux generated by an infinitely narrow solenoid (14). Signatures of this localized flux have been observed in graphene through measurements of a half-integer shift in the positions of quantum Hall plateaus (15, 16), the phase of Shubnikov-de Haas oscillations (15, 16), and the polarization

dependence in photoemission spectra (17, 18). A similar π flux also plays a crucial role in the nuclear dynamics of molecules featuring conical intersections of energy surfaces (2). Our direct detection of the singular π flux demonstrates the capability of atom interferometry to detect Berry flux features that are challenging to observe by alternative techniques based on transport measurements (7, 8, 19–21), paving the way to full topological characterization of optical lattice systems (20–27).

The effect of Berry curvature in our interferometer is analogous to the Aharonov-Bohm effect, in which an electron wave packet is split into two parts that encircle a given area in real space (Fig. 1A). Any magnetic flux through the enclosed area gives rise to a measurable phase difference between the two components. For a single Bloch band in the reciprocal space of a lattice system, an analog of the magnetic field is the Berry curvature Ω_n (Eq. 1), which we probe by forming an interferometer on a closed path in reciprocal space (Fig. 1B). The geometric phase acquired along the path can be calculated from the Berry connection \mathcal{A}_n , the analog of the magnetic vector potential. For a lattice system with Bloch waves $\psi_{\mathbf{k}}^n(\mathbf{r}) = e^{i\mathbf{k}\cdot\mathbf{r}} u_{\mathbf{k}}^n(\mathbf{r})$ with quasimomentum \mathbf{k} in the n th band and the cell-periodic part of the wave function $u_{\mathbf{k}}^n(\mathbf{r})$, the Berry

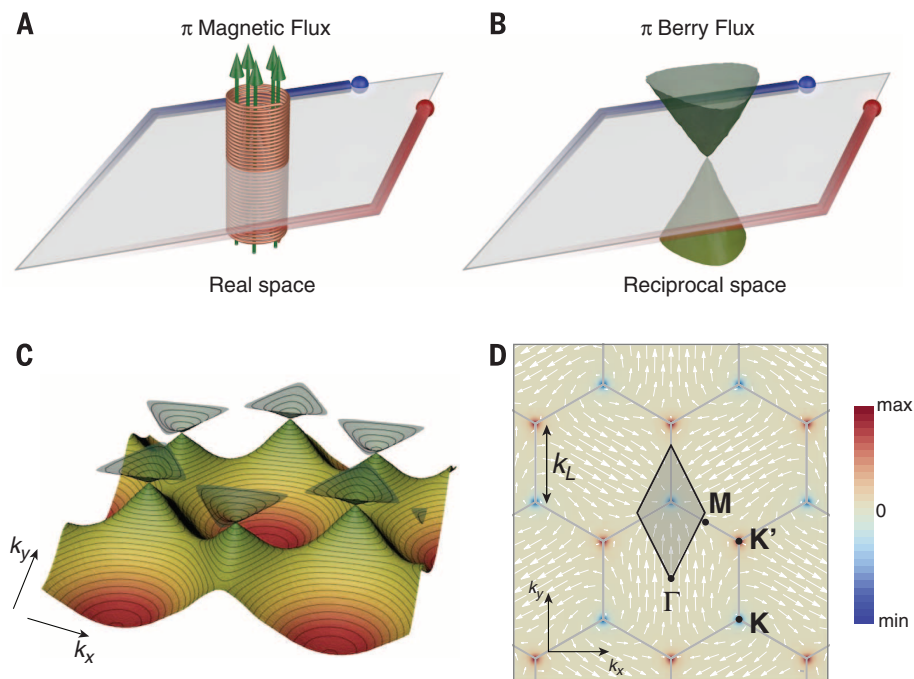


Fig. 1. Aharonov-Bohm analogy and geometric properties of the hexagonal lattice. In the Aharonov-Bohm effect (A), electrons encircle a magnetic flux in real space, whereas in our interferometer (B), the particles encircle the π Berry flux of a Dirac point in reciprocal space. In both cases, the flux through the interferometer loop gives rise to a measurable phase. (C) Dispersion relation of the hexagonal lattice, showing the conical intersection between the first and second band at the Dirac points. (D) Berry curvature of the first band calculated in the tight-binding regime with a gap of $\Delta = 0.5 J$ for visualization purposes. Dirac points are located at the corners (K and K' points) of the BZ (gray hexagons). White arrows are a pseudospin representation of the Bloch states; lengths of the arrows indicate the energy gap in the two-band model. Also shown is a typical interferometer path (black diamond).

¹Fakultät für Physik, Ludwig-Maximilians-Universität München, Schellingstrasse 4, 80799 Munich, Germany.

²Max-Planck-Institut für Quantenoptik, Hans-Kopfermann-Strasse 1, 85748 Garching, Germany. ³Department of Physics, Stanford University, Stanford, CA 94305, USA.

*Corresponding author. E-mail: ulrich.schneider@lmu.de

connection is given by $\mathbf{A}_n(\mathbf{k}) = i\langle u_{\mathbf{k}}^n | \nabla_{\mathbf{k}} | u_{\mathbf{k}}^n \rangle$. Accordingly, the phase along a closed loop in reciprocal space is (1, 2)

$$\varphi_{\text{Berry}} = \oint_C \mathbf{A}_n(\mathbf{k}) d\mathbf{k} = \int_S \Omega_n(\mathbf{k}) d^2\mathbf{k} \quad (1)$$

where S is the area enclosed by the path $C = \partial S$, and $\Omega_n = \nabla_{\mathbf{k}} \times \mathbf{A}_n(\mathbf{k})$ is the Berry curvature (color shading in Fig. 1D) (4). Although neither the magnetic vector potential nor the Berry connection is uniquely defined, the geometric phase acquired along a closed loop is gauge independent (1) and is therefore a measurable observable that encodes information on the geometrical properties of a Bloch band.

We implemented the graphene-like hexagonal optical lattice for ultracold ^{87}Rb atoms by superimposing three linearly polarized blue-detuned running waves at $120(1)^\circ$ angles (Fig. 2A). The resulting dispersion relation includes two nonequivalent Dirac points with opposite Berry flux located at \mathbf{K} and \mathbf{K}' , which are repeated in every Brillouin zone (BZ) (Fig. 1D). The origin of the π Berry flux lies in the bipartite structure of the hexagonal lattice (12): Because the unit cell contains two nonequivalent lattice sites A and B (Fig. 2A), the Bloch wave of the lowest band is constrained to the equatorial plane of its Bloch sphere by a combination of time-reversal invar-

iance and the inversion symmetry of the lattice, and its phase winds around each Dirac point as shown in Fig. 1D. The spinor Bloch wave, just as a real spin-1/2 particle in a slowly rotating magnetic field, therefore acquires a geometric phase of π along any trajectory enclosing a single Dirac point. The Berry curvature is thus confined to a perfectly localized π Berry flux, $\Omega_n = \pm\pi\delta(\mathbf{k} - \mathbf{K}^{(\prime)})$, provided the aforementioned symmetries hold (13). Generically, the inversion symmetry may be broken by a slight ellipticity of the lattice beam polarizations, which introduces a small energy offset Δ between the A and B sites (6). Such an offset opens a small gap at the Dirac points and spreads the Berry curvature over a finite range

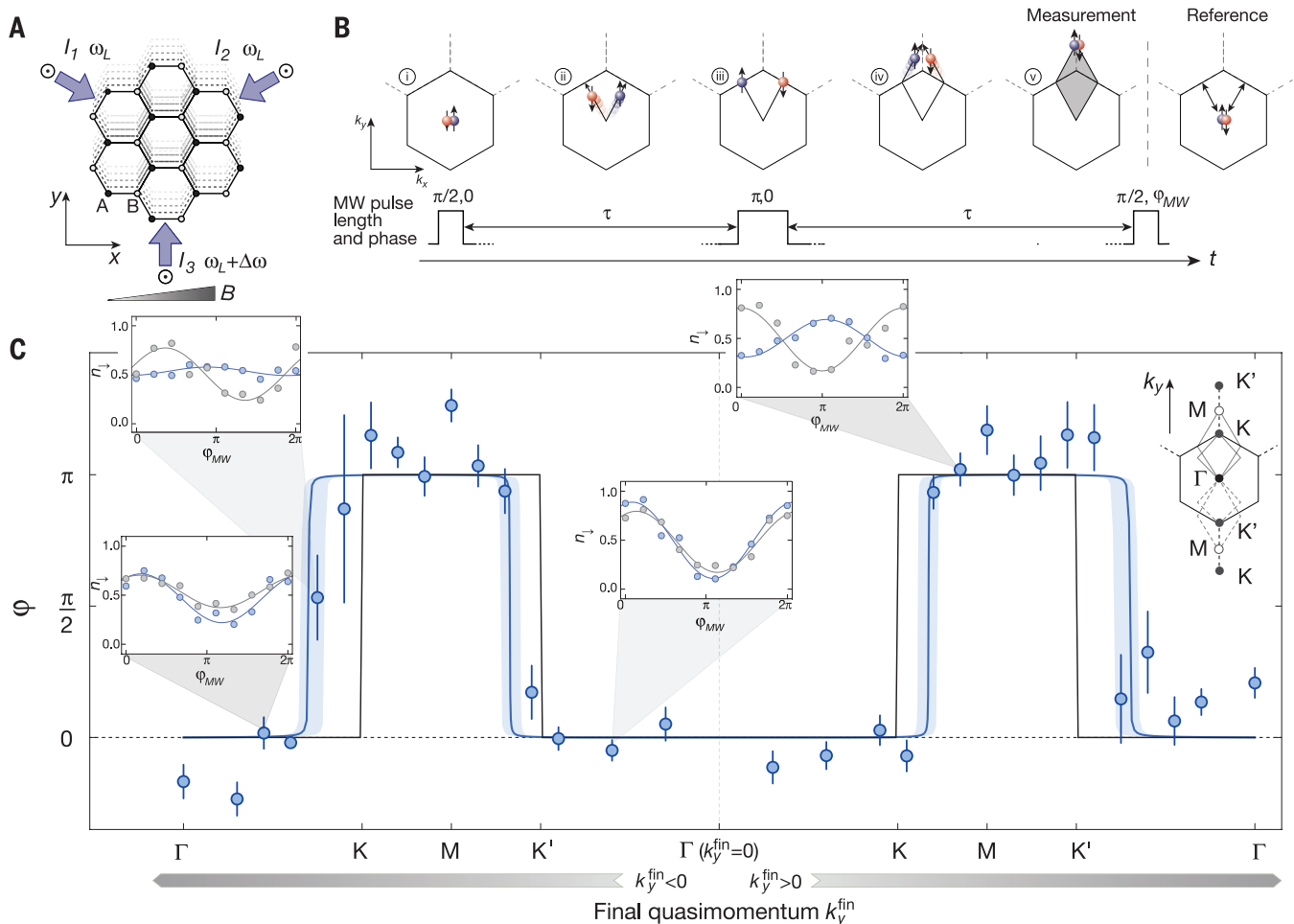


Fig. 2. Momentum-resolved detection of Berry flux at the Dirac points.

(A) Sketch of the hexagonal lattice in real space with A (B) sites denoted by solid (open) circles. The lattice is realized by interfering three laser beams (arrows) of wavelength λ_L , intensity I_i , and frequency ω_L , with linear out-of-plane polarizations. A linear frequency sweep of the third lattice beam creates a uniform lattice acceleration along the y direction. A magnetic field gradient $B' = 9.0(1)$ G/cm along the x axis creates an additional spin-dependent force. (B) Interferometer sequence. Hexagons indicate the first BZ, and red (blue) spheres are atoms in the $|\downarrow\rangle$ ($|\uparrow\rangle$) state. The duration of the interferometer sequence is $2\tau = 1.6$ ms for all measurements. (C) Summary of phase shifts measured relative to the zero-area reference interferometer for different final quasimomenta k_y^{fin} . Error bars denote fit uncertainties or standard deviations

in case of averages. Lines are ab initio theory using a full band structure calculation with no momentum spread $\sigma_k = 0$ and perfectly localized Berry curvature $\delta k_\Omega = 0$ (black) or $\sigma_k = 0.21 k_L$ and $\delta k_\Omega \approx 10^{-4} k_L$ (blue). Here, the shift in the phase jump results from the momentum spread σ_k (13), the broadening of the edges is caused by δk_Ω , and the shaded area accounts for a variation in $\sigma_k = 0.14 - 0.28 k_L$. Insets show the fraction of atoms n_+ detected in state $|\downarrow\rangle$ as a function of the phase φ_{MW} for selected quasimomenta. Measurement loop data are shown in blue, and zero-area reference data are shown in gray, with corresponding sinusoidal fits. The contrast is limited by inhomogeneous broadening of the microwave transition, the finite momentum spread of the condensate, and, for large final quasimomenta, the dynamical instability of the Gross-Pitaevskii equation (32).

of quasimomenta (Fig. 1D). By probing for a spread in Berry curvature, we can place a bound on imperfections in the lattice, while simultaneously benchmarking the resolution of our interferometer.

The interferometer sequence (Fig. 2B) begins with the preparation of an almost pure ^{87}Rb BEC in the state $|\uparrow\rangle = |F=2, m_F=1\rangle$ at quasimomentum $\mathbf{k} = \mathbf{0}$ in a $V_0 = 1 E_r$ deep lattice, where $E_r = \hbar^2/(2m\lambda_L^2) \approx \hbar \times 4$ kHz is the recoil energy and \hbar is Planck's constant. A resonant $\pi/2$ -microwave pulse creates a coherent superposition of $|\uparrow\rangle$ and $|\downarrow\rangle = |F=1, m_F=1\rangle$ states (i). Next, a spin-dependent force from a magnetic field gradient and an orthogonal spin-independent force from lattice acceleration (Fig. 2A) move the atoms adiabatically along spin-dependent paths in reciprocal space (ii) (28). The two spin components move symmetrically about a symmetry axis of the dispersion relation. After an evolution time τ , a microwave π pulse swaps the states $|\downarrow\rangle$ and $|\uparrow\rangle$ (iii). The two atomic wave packets now experience opposite magnetic forces in the x direction, such that both spin components arrive at the same quasimomentum k_y^{fin} after an additional evolution time τ (iv). At this point, the state of the atoms is given by $|\psi^{\text{fin}}\rangle \propto |\uparrow, k_y^{\text{fin}}\rangle + e^{i\varphi} |\downarrow, k_y^{\text{fin}}\rangle$ with relative phase φ . A second $\pi/2$ -microwave pulse with a variable phase φ_{MW} closes the interferometer (v) and converts the phase information into spin population fractions $n_{\uparrow, \downarrow} \propto 1 \pm \cos(\varphi + \varphi_{\text{MW}})$, which are measured by standard absorption imaging after a Stern-Gerlach pulse and time of flight.

The phase difference φ at the end of the interferometer sequence consists of the geometric phase and any difference in dynamical phases between the two paths of the interferometer. Ideally, the dynamical contribution should vanish because of the symmetry of the paths and the use of the spin-echo sequence (13). To ascertain that the measured phase is truly of geometric origin, we additionally employ a “zero-area” reference interferometer, comprising a V-shaped path (Fig. 2B) produced by reversing the lattice acceleration after the π -microwave pulse of Fig. 2B (iii).

We locate the Berry flux of the Dirac cone by performing a sequence of measurements in which we vary the region enclosed by the interferometer. This is achieved by varying the lattice acceleration at constant magnetic field gradient to control the final quasimomentum k_y^{fin} ($k_x^{\text{fin}} = 0$) of the diamond-shaped measurement loop. The resulting phase differences between measurement and reference loops are shown in Fig. 2C. When one Dirac point is enclosed in the measurement loop, we observe a phase difference of $\varphi \approx \pi$. In contrast, we find the phase difference to vanish when enclosing zero or two Dirac points. We find very good agreement between our data and a theoretical model that includes the finite spread σ_k in the initial momentum of the weakly interacting BEC (blue curve in Fig. 2C) (13). Because of this spread, each atom has sampled a slightly different path in momentum space and may therefore have acquired a different geometric phase. Once the

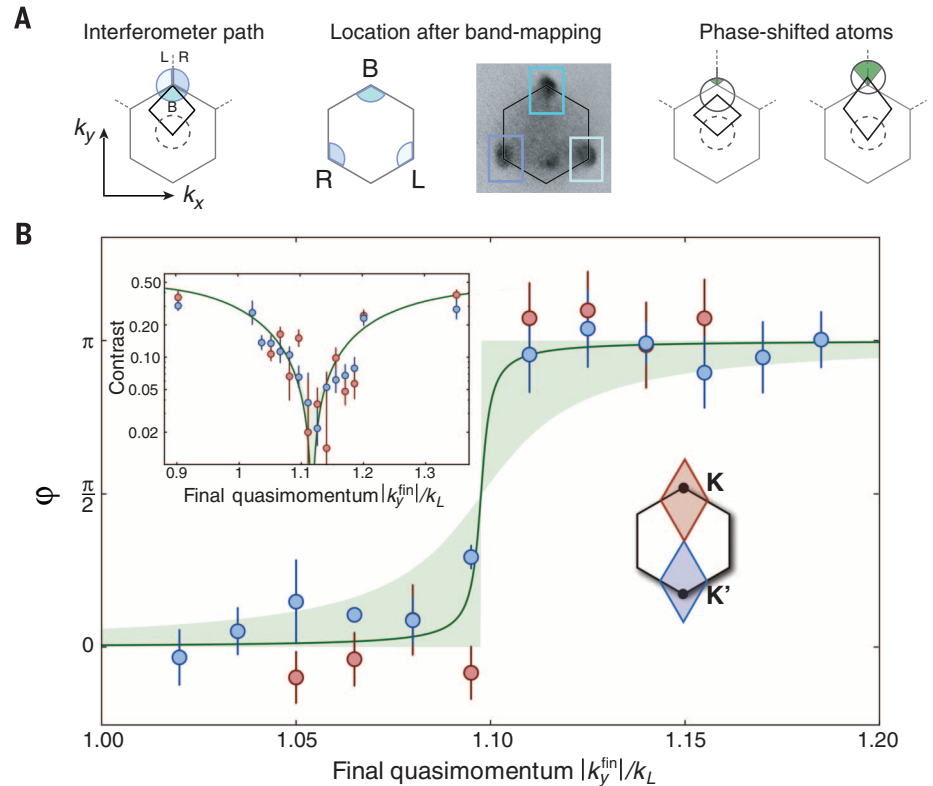


Fig. 3. Self-referenced interferometry at the Dirac point. (A) (Left) Interferometer path closing at the K point. Because of the initial momentum spread, the cloud (circle with colored sectors, not to scale) is split by the edges of the BZ. (Middle) Band mapping spatially separates the three different parts of the cloud onto three corners of the first BZ (schematic and image, where cloud sizes are dominated by in situ size). (Right) The fraction of atoms for which the Dirac point lies within the interferometer loop (green sectors) increases with final quasimomentum k_y^{fin} . (B) Phase differences between atoms that have crossed the band edge (sectors L and R) and those that have not (sector B) versus final quasimomentum k_y^{fin} for paths close to the K (K') point in red (blue). The shaded region indicates a range $\delta k_\Omega = 0 - 12 \times 10^{-4} k_L$ for the spread in Berry curvature, whereas the line is calculated for $\delta k_\Omega \approx 10^{-4} k_L$ using the model described in (13), corresponding to an A-B offset of $\Delta \approx \hbar \times 3$ Hz. The inset shows the contrast $(n_i^{\text{max}} - n_i^{\text{min}})/(n_i^{\text{max}} + n_i^{\text{min}})$ of the interference fringes of the full cloud. Theory line and shading are for the same parameters as in the main graph and include only geometrical phases (13). All calculations assume $\sigma_k = 0.15 k_L$.

Dirac point lies within the interferometer area for exactly half of the atoms, the first phase jump occurs. Because of the small opening angle of the chosen interferometer path ($\sim 70^\circ$), this happens slightly later than in the ideal case of $\sigma_k = 0$ (black curve in Fig. 2C). Although σ_k thereby affects the positions of the π phase jumps, it does not limit their sharpness. Indeed, the data are fully consistent with the behavior expected for an inversion-symmetric lattice, where it is impossible to identify the sign of the singular Berry flux ($\pm\pi$). Small deviations of the phases from 0 or π can be attributed to an imperfect alignment of the magnetic field gradient, magnetic field fluctuations, or an imperfect lattice geometry (13). These systematic effects are particularly relevant close to the phase jump, where the contrast is minimal and can influence the perceived direction of the phase jump.

To minimize systematic errors and improve our measurement precision, we performed self-

referenced interferometry close to the Dirac points. As illustrated in Fig. 3A, a standard band-mapping technique (29) projects those sectors of the cloud that have (left and right) or have not (bottom) crossed the edge of the BZ onto three different corners of the first BZ, such that we can measure their acquired phases independently. Combining these measured phases to $\varphi = (\varphi_L + \varphi_R)/2 - \varphi_B$, where φ_L , φ_R , and φ_B refer to the phases of the three sectors, eliminates the need for a separate reference measurement and significantly reduces sensitivity to drifts in the experiment. The resulting phase again shows a sudden jump from 0 to π (Fig. 3B). The position of the phase jump is in excellent agreement with a simple single-band model (13) that includes an initial momentum spread of $\sigma_k = 0.15(1)k_L$, consistent with an independent time-of-flight measurement. Notably, the phase jump occurs within a very small quasimomentum range of $< 0.01 k_L$, and an arctangent fit to the

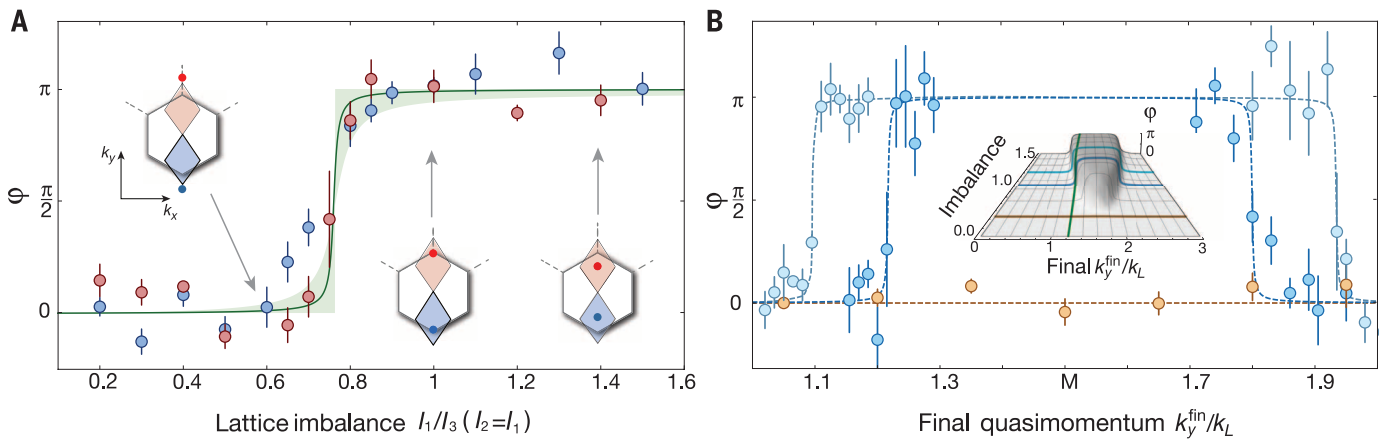


Fig. 4. Mapping the movement of Berry flux under distortion of the lattice. (A) Phase difference between the zero-area reference loop and measurement loop versus lattice imbalance for a fixed final quasimomentum $k_y^{\text{fin}} = \pm 1.2k_L$ near \mathbf{K} (red) or \mathbf{K}' (blue). Red and blue dots in the insets give the location of Dirac points for the indicated imbalances. Theory curve is calculated for lattice depth $V_0 = 1E_n$, momentum spread $\sigma_k = 0.15k_L$, and $\delta k_\Omega \approx 10^{-4}k_L$. Shaded area corresponds to $\delta k_\Omega = 0 - 12 \times 10^{-4}k_L$. (B) Self-referenced phase near \mathbf{K} and \mathbf{K}'

for an imbalance $I_{1,2}/I_3 = 1.0$ and $I_{1,2}/I_3 = 0.7$ in light and dark blue, highlighting the shift in the location of Berry flux. Phases are measured as in Fig. 3. Orange data are phase differences between the measurement and reference loops for an imbalance of $I_{1,2}/I_3 = 0.2$, where no phase shift is observed. Curves are guides to the eye. The inset shows the calculated Berry phase for loops with various final k_y^{fin} and lattice imbalances using the same σ_k and δk_Ω as above. Colored lines indicate parameters explored in the measurements.

experimental data gives a phase step of $\varphi = 0.95(10)\pi$. Both results are compatible with a perfectly localized and quantized π Berry flux.

To constrain the possible spread in Berry curvature, we analyze not only the phase (Fig. 3B) but also the contrast of the interference fringes (Fig. 3B, inset). The location of the Dirac cone manifests itself through a pronounced minimum in the interference contrast. The sharpness of the phase jump and the strong reduction of contrast down to our detection limit demonstrate that the interferometric protocol can map the Berry curvature with very high resolution. By comparing the experimental contrast with our theoretical model (13), we find an upper bound for the spread of the Berry curvature around the Dirac cone of $\delta k_\Omega \leq 6 \times 10^{-4}k_L$ (half-width at half maximum). This corresponds to a maximal A-B site offset of $\Delta \leq \hbar \times 12$ Hz and a ratio of energy gap at the Dirac cone to bandwidth of $\leq 1 \times 10^{-3}$. The steepness of the phase jump in Fig. 3B suggests an even stronger localization of the Berry curvature on the order of $\delta k_W \approx 10^{-4}k_L$ ($\Delta \approx \hbar \times 3$ Hz). Although the vanishing band gap precludes performing a perfectly adiabatic measurement in the immediate proximity of the Dirac point, the population in the second band is constrained by independent measurements to be $\leq 20\%$ of the total atom number (13).

To verify the method's sensitivity to changes in Berry flux, we performed interferometry in a modified lattice potential. Changing the power of two lattice beams (I_1 and I_2) relative to the third (I_3) deforms the lattice structure but preserves time-reversal and inversion symmetry. With decreasing $I_{1,2}/I_3 < 1$, the Dirac points and the associated fluxes move along the symmetry axis of the interferometer loop (I2) (insets of Fig. 4A). Nonetheless, the Berry flux singularities remain protected by symmetry until the Dirac points merge and annihilate (23, 30, 31). By using a fixed

measurement loop that encloses one Dirac point in the intensity-balanced case, we can measure the change of the geometric phase as we imbalance the lattice beam intensities. The measured Berry phases drop from π to 0 as the Dirac point moves out of the loop, in very good agreement with ab initio calculations (see Fig. 4A). To map the location of the Berry flux in the imbalanced lattice, we again use the self-referenced interferometry of Fig. 3. As shown in Fig. 4B, imbalancing the lattice by decreasing $I_{1,2}/I_3$ narrows the range of final quasimomenta for which the interferometer encloses a single π flux, thereby shifting both the upward and downward phase jumps toward the M point. For strong imbalance ($I_{1,2}/I_3 = 0.2$), the two Dirac points have annihilated, and hence no phase jump is observed for any loop size. At intermediate imbalance ($I_{1,2}/I_3 = 0.7$), the position of the phase jump at $k_y^{\text{fin}} = 1.2k_L$ is in very good agreement with theory, whereas deviations of $\approx 10\%$ from the calculated value in the position of the second phase jump can likely be attributed to a combination of geometric imperfections, nonadiabaticity of motion at the Dirac point, and the dynamical instability of the Gross-Pitaevskii equation (32), which results in an additional broadening of the quasimomentum distribution. The latter effects can be suppressed by combining slower ramps with the use of a Feshbach resonance in an atomic species such as ^{39}K (33).

Our Aharonov-Bohm-type interferometer enabled us to detect a localization of Berry flux to better than 10^{-6} of the Brillouin zone area. This method allows one to fully resolve the Berry curvature distribution of a single Bloch band by combining local measurements of the geometric phases along small paths, thereby enabling the full reconstruction of topological invariants such as Chern numbers. The method can readily be applied to a variety of optical lattices and other

physical settings such as polariton condensates (34). Multiband extensions of this work can enable measurements of Wilson loops and off-diagonal (non-Abelian) Berry connections and thus provide a framework for determining the complete geometric tensor of Bloch bands in periodic structures (35). Controlled application of non-Abelian Berry phases would furthermore constitute a key step toward holonomic quantum computation (36). Even within a single topologically trivial band, the possibility of preparing a BEC or Fermi sea at finite quasimomentum should enable the observation of transient Hall responses due to local Berry curvature and, combined with the possibility of performing quantum quenches and the control of interactions, is expected to lead to novel many-body phenomena (37). Finally, the highly nonlinear phase jump we have observed at the Dirac point may find application in precision force sensing (38).

REFERENCES AND NOTES

1. M. V. Berry, *Proc. R. Soc. London Ser. A* **392**, 45–57 (1984).
2. A. Shapere, F. Wilczek, *Advanced Series in Mathematical Physics: Volume 5, Geometric Phases in Physics* (World Scientific, Singapore, 1989).
3. Y. Aharonov, D. Bohm, *Phys. Rev.* **115**, 485–491 (1959).
4. D. Xiao, M.-C. Chang, Q. Niu, *Rev. Mod. Phys.* **82**, 1959–2007 (2010).
5. D. J. Thouless, M. Kohmoto, M. P. Nightingale, M. den Nijs, *Phys. Rev. Lett.* **49**, 405–408 (1982).
6. M. Z. Hasan, C. L. Kane, *Rev. Mod. Phys.* **82**, 3045–3067 (2010).
7. H. Price, N. Cooper, *Phys. Rev. A* **85**, 033620 (2012).
8. A. Dauphin, N. Goldman, *Phys. Rev. Lett.* **111**, 135302 (2013).
9. D. A. Abanin, T. Kitagawa, I. Bloch, E. Demler, *Phys. Rev. Lett.* **110**, 165304 (2013).
10. P. Hauke, M. Lewenstein, A. Eckardt, *Phys. Rev. Lett.* **113**, 045303 (2014).
11. M. Atala *et al.*, *Nat. Phys.* **9**, 795–800 (2013).
12. A. H. Castro Neto, F. Guinea, N. M. R. Peres, K. S. Novoselov, A. K. Geim, *Rev. Mod. Phys.* **81**, 109–162 (2009).
13. See the supplementary materials on Science Online.
14. G. P. Mikitik, Y. V. Sharlai, *Phys. Rev. Lett.* **82**, 2147–2150 (1999).

15. Y. Zhang, Y.-W. Tan, H. L. Stormer, P. Kim, *Nature* **438**, 201–204 (2005).
16. K. S. Novoselov *et al.*, *Nature* **438**, 197–200 (2005).
17. Y. Liu, G. Bian, T. Miller, T.-C. Chiang, *Phys. Rev. Lett.* **107**, 166803 (2011).
18. C. Hwang *et al.*, *Phys. Rev. B* **84**, 125422 (2011).
19. M. Aidelburger, *et al.*, *Nat. Phys.* **2014**, 10.1038/nphys3171 (2014).
20. G. Jotzu *et al.*, *Nature* **515**, 237–240 (2014).
21. I. B. Spielman, *Annalen der Physik* **525**, 797–807 (2013).
22. M. Aidelburger *et al.*, *Phys. Rev. Lett.* **107**, 255301 (2011).
23. L. Tarruell, D. Greif, T. Uehlinger, G. Jotzu, T. Esslinger, *Nature* **483**, 302–305 (2012).
24. J. Struck *et al.*, *Nat. Phys.* **9**, 738–743 (2013).
25. M. Aidelburger *et al.*, *Phys. Rev. Lett.* **111**, 185301 (2013).
26. H. Miyake, G. A. Siviloglou, C. J. Kennedy, W. C. Burton, W. Ketterle, *Phys. Rev. Lett.* **111**, 185302 (2013).
27. N. Goldman, G. Juzeliunas, P. Ohberg, I. B. Spielman, *Rep. Prog. Phys.* **77**, 126401 (2014).
28. M. Ben Dahan, E. Peik, J. Reichel, Y. Castin, C. Salomon, *Phys. Rev. Lett.* **76**, 4508–4511 (1996).
29. M. Greiner, I. Bloch, O. Mandel, T. W. Hänsch, T. Esslinger, *Phys. Rev. Lett.* **87**, 160405 (2001).
30. S.-L. Zhu, B. Wang, L.-M. Duan, *Phys. Rev. Lett.* **98**, 260402 (2007).
31. P. Dieltz, F. Piéchon, G. Montambaux, *Phys. Rev. Lett.* **100**, 236405 (2008).
32. L. Fallani *et al.*, *Phys. Rev. Lett.* **93**, 140406 (2004).
33. C. D'Errico *et al.*, *New J. Phys.* **9**, 223 (2007).
34. I. Carusotto, C. Ciuti, *Rev. Mod. Phys.* **85**, 299–366 (2013).
35. F. Grusdt, D. Abanin, E. Demler, *Phys. Rev. A* **89**, 043621 (2014).
36. P. Zanardi, M. Rasetti, *Phys. Lett. A* **264**, 94–99 (1999).
37. S. A. Parameswaran, R. Roy, S. L. Sondhi, *C. R. Phys.* **14**, 816–839 (2013).
38. A. K. Tuchman, M. A. Kasevich, *Phys. Rev. Lett.* **103**, 130403 (2009).

ACKNOWLEDGMENTS

We acknowledge technical assistance by M. Boll, H. Lüschen, and J. Bernarhoff during the setup of the experiment and thank E. Demler, D. Abanin, and X.-L. Qi for helpful discussions. We acknowledge financial support by the Deutsche Forschungsgemeinschaft (FOR801), the European Commission (UQUAM), the U.S. Defense Advanced Research Projects Agency Optical Lattice Emulator program, the Nanosystems Initiative Munich, and the Alfred P. Sloan Foundation.

SUPPLEMENTARY MATERIALS

www.sciencemag.org/content/347/6219/288/suppl/DC1
Supplementary Text
Figs. S1 to S3
References (39–49)

22 July 2014; accepted 5 December 2014
Published online 18 December 2014;
10.1126/science.1259052

INTERFACIAL SOLVENTS

Universal solvent restructuring induced by colloidal nanoparticles

Mirijam Zobel,^{1*} Reinhard B. Neder,¹ Simon A. J. Kimber^{2*}

Colloidal nanoparticles, used for applications from catalysis and energy applications to cosmetics, are typically embedded in matrixes or dispersed in solutions. The entire particle surface, which is where reactions are expected to occur, is thus exposed. Here, we show with x-ray pair distribution function analysis that polar and nonpolar solvents universally restructure around nanoparticles. Layers of enhanced order exist with a thickness influenced by the molecule size and up to 2 nanometers beyond the nanoparticle surface. These results show that the enhanced reactivity of solvated nanoparticles includes a contribution from a solvation shell of the size of the particle itself.

Bulk liquids have long been known to show short-range order. The original method of choice was x-ray scattering, which was used by Zachariasen in 1935 to study the short-range order between solvent molecules (1). Alcohol molecules were shown to form a hydrogen-bonded network within the bulk solvent (2–4), and short alkanes were found to align in parallel within domains of ~2 nm (5). More recently, the influence of hard planar walls on bulk liquids has been investigated (6–8). Together with force measurements (7, 8), x-ray scattering confirmed that an exponentially decaying oscillatory density profile is established near the interface (9). With the advent of synchrotron radiation sources, Magnussen *et al.* showed by use of x-ray reflectivity that even liquid mercury orders at a flat solid interface in exactly the same way (9). More recent examples of such ordering phenomena at interfaces include the restructuring of nonpolar n-hexane (10), the assembly of fluorinated ionic liquids at sapphire surfaces (11),

and the exponentially decaying surface segregation profiles in Cu₃Au alloy interfaces (12). These restructuring phenomena—in particular, the interlayer spacings and decay lengths—are closely related to the local ordering in the bulk liquid (9, 12).

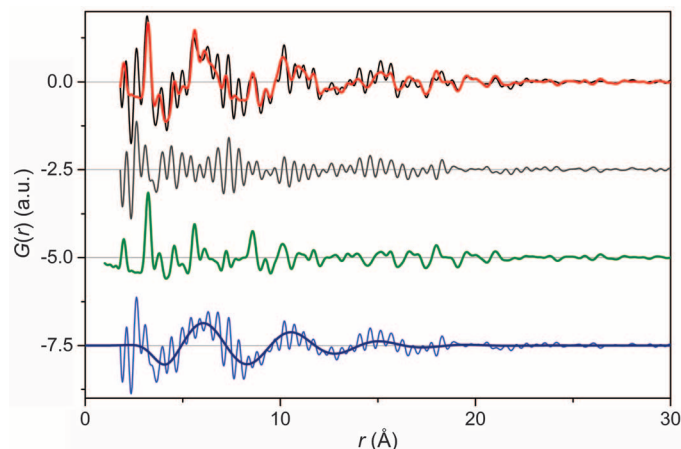
Although the reorganization of solvent molecules around isolated cations in solution has also been explored (13, 14), comparable studies on solvated nanoparticles (NPs) are rare, in par-

ticular for nonaqueous solvent (15–17). Solvent molecules are expected and have theoretically been modeled (15, 16) to rearrange at the liquid-NP interface, although no definitive experimental proof exists so far. For bulk planar surfaces (6–8) and ions (13, 14), such enhanced order is well understood. Here, we report a synchrotron x-ray scattering study of a variety of as-synthesized and commercial NPs in polar and nonpolar solvents. We show enhanced ordering of solvent molecules at the NP surface that extends several layers into the bulk liquid. This effect is largely independent of the capping agent, solvent polarity, and particle size.

We systematically redispersed different types of metal and metal oxide NPs in polar and nonpolar organic solvents (18). We studied the influence of the solvent molecule size within the series of primary alcohols (methanol, ethanol, and 1-propanol) and the effect on nonpolar solvents with hexane. Fourier transformation of high-energy x-ray scattering patterns yielded the pair distribution functions (PDFs), histograms of all interatomic distances within a sample. Data treatment includes the subtraction of diffraction data of the respective pure solvent so that the signal from the bulk solvent is subtracted before the Fourier transformation. The

Fig. 1. Fit to the PDF of redispersed ZnO NPs with citrate ligands in propanol.

Experimental d-PDF of ZnO NPs (black) and their fit (red), showing the overall difference of the fit (gray), the contribution of the NP (green), and the contribution and fit of the restructured solvent (blue) in offset for means of clarity. The contribution of the restructured solvent (blue) is the dd-PDF of the experimental, background-corrected d-PDF (black) and the NP (green).



¹Department of Physics, Lehrstuhl für Kristallographie und Strukturphysik, Friedrich-Alexander University Erlangen-Nürnberg, Staudtstrasse 3, 91058 Erlangen, Germany. ²European Synchrotron Radiation Facility, 71 Avenue des Martyrs, 38000 Grenoble, France.

*Corresponding author. E-mail: mirijam.zobel@fau.de (M.Z.); kimber@esrf.fr (S.A.J.K.)